Solar Active Region Flux Fragmentation, Subphotospheric Flows, and Flaring

Richard C. Canfield and Alexander J. B. Russell[1]

canfield@physics.montana.edu, ar51@st-andrews.ac.uk

Physics Department, Montana State University, Bozeman MT 59717

ABSTRACT

We explore the properties of the fragmentation of magnetic flux in solar active regions. We apply gradient-based tessellation to magnetograms of 59 active regions to identify flux fragments. First, we find that the distribution function of flux fragments in these regions is highly consistent with lognormal form, which is the most direct evidence yet obtained that repeated random bifurcation dominates fragmentation and coalescence in all active regions. Second, we apply non-parametric statistical methods to the variance of the lognornal distribution of fragment flux, the flare X-ray energy output of the active regions, and kinetic helicity measurements in the upper convection zone (Komm *et al.* 2005) to show that there is no significant statistical relationship between the amount of fragmentation of an active region's flux at photospheric levels and the amplitude of either its average kinetic helicity density in the upper convection zone or its X-ray flare energy output.

Subject headings: Sun: magnetic fields — Sun: flares — Sun: helioseismology

1. INTRODUCTION

Magnetic flux is thought to be generated below the convection zone and rise buoyantly in loops of Ω shape through the turbulent convective environment that is found there (Fan 2004). The emergence of the apex of an Ω loop through the photosphere accounts for many of the observed properties of solar active regions (Canfield 1999; Fisher *et al.* 2000; Nandy 2006). During the passage of these Ω loops through the convection zone, convective

[1]Also Departments of Mathematics and Theoretical Physics, University of St. Andrews, Scotland.

turbulence is believed to have several important effects, including distortion and fragmentation. Distortion tends to generate various forms of magnetic helicity (Brown *et al.* 1999), since the Coriolis force makes the paths of rising and falling convective elements helical. Longcope *et al*. (1988) showed that buffeting by helical turbulence writhes Ω loops as they rise through the convection zone, which produces twist through helicity conservation. Emergence of magnetic helicity into the corona, in the form of various components of magnetic helicity, has been argued to play an important role in eruptive solar flares and coronal mass ejections (Moon *et al.* 2002; Nindos and Andrews 2004; Leka *et al.* 2005; Longcope *et al.* 2007).

Such distortion of the axes of Ω loops as they rise through the convection zone may or may not be related to fragmentation. Bogdan *et al*. (1988) found a lognormal distribution of the umbral area of more than 24,000 sunspots observed in white light. A lognormal distribution strongly implies repeated random bifurcation of the parent flux tubes. A more direct measurement, using the same methods as the present study, was carried out by Abramenko and Longcope (2005) . Although they studied only two active regions, they identified flux fragments in magnetograms, not white-light proxies. They found that the fragment flux distribution function in these regions was of lognormal form in the flux range $\Phi > 10^{19}$ Mx; neither exponential nor power law functions provided a consistent fit to their observations. The present paper represents the extension of this work to a statistically significant number of active regions.

The process of repeated random bifurcation may or may not coincide with distortion and the generation of twist or writhe. Under some circumstances, the dominant consequence of convective turbulence may be fragmentation (say, when convective elements are small in size compared to the diameter of the tube, as is the case in the upper convection zone (Fan *et al.* 1993)). On the other hand, the dominant consequence may be axial writhing when the size of the convective elements is large compared to the loop diameter, but small compared to the loop length.

Our work is further motivated by recent studies of helical flows in the upper convection zone. Through local helioseismology, one can infer the presence of flows through their effects on waves observable in the neighborhood of active regions (Hill 1988; Haber *et al.* 2000). Thereby, one can infer the spatially averaged value of the kinetic helicity density $\langle k \rangle = v \cdot (\nabla \times v)$ of flows of velocity v at various depths in the upper convection zone. One of the most interesting results to come recently from local helioseismology is a relation between flaring in ARs and the average kinetic helicity of surrounding flows in the upper convection zone (Komm *et al.* 2005). Since one might expect large values of kinetic helicity to be associated with strong flows, and in turn strong fragmentation, we seek to determine through observations whether such a relationship exists.

2. DATA AND ANALYSIS

We chose for study 59 active regions, all of which were present during two solar rotations – Carrington Rotation 1982 (2001 October 17 - November 12) and CR 1988 (2002 March 30 - April 26). The AR vary widely in unsigned flux and size, from 2.06×10^{20} to 1.38×10^{22} Mx and from 2.01×10^{18} to 1.16×10^{20} cm^2. By design, all these AR have been studied by Komm and collaborators (Komm *et al.* 2005), who determined the subsurface kinetic helicity density for each AR from GONG and MDI data. These authors use ring-diagram analysis (Hill 1988; Haber *et al.* 2000); their measurements average over a 15° region. Komm and collaborators found a relationship between $\langle k \rangle$ and the total X-ray flare energy output of these ARs, determined by summing the GOES flux of all flares recorded within them. In this work we also used GOES measurements to determine independently the X-ray flare energy output, following the methods described elsewhere (Nandy *et al.* 2003). As one might expect from the wide range of AR flux and size values, values of the measured GOES integrated flare energy flux per AR also vary widely, from 6.32×10^{-4} to 7.90×10^{-1} J m^{-2}.

Our primary data for these 59 ARs are magnetograms derived from medium resolution full disk Kitt Peak magnetograms (2″ pixels, λ868.8 nm), obtained from the NSO/KP Vacuum Telescope ftp archive (http://nsokp.nso.edu/dataarch.html). For each AR in the study, the daily full disk magnetogram showing the region on the day when it was closest to disk center was selected, to best approximate the vertical magnetic field with the best effective spatial resolution. Almost all regions from these Carrington Rotations were included in our study; the only exceptions occurred when these data were not available within one day of the AR's crossing of the central meridian.

2.1. Tessellation of the Magnetograms

The flux of active regions is patently intermittent and fragmented (Fig. 1). Our expectation is that this fragmentation is a consequence of the passage of the AR's parent flux tube through the convection zone on its journey to the surface. One model for this process is that of repeated, random bifurcation, in which an initial flux tube is divided into two fractions at random, many times. This produces flux fragments with a lognormal distribution (Monin and Yaglom 1975; Bogdan *et al.* 1988; Abramenko and Longcope 2005), which is consistent with observations of sunspot umbrae (Bogdan *et al.* 1988). Other processes can come into play in AR evolution, e.g. coalescence, but the fact that our observations below show a lognormal distribution for a statistically significant number of active regions strongly implies that such fragmentation is dominant.

Several earlier authors (Schrijver *et al.* 1997; Barnes *et al.* 2005) have developed gradient-based tessellation schemes to identify individual fragments of flux within magnetograms. Guided by their work, we wrote such a tessellation code and applied it to the Kitt Peak magnetograms. A pixel is considered to belong to a flux fragment if, and only if, the absolute value of magnetic field in that pixel exceeded a given threshold - the "tessellation threshold". Every pixel satisfying this constraint is then considered in order of unsigned field, greatest first. Clearly, the global maximum in magnetic field lies at the heart of a flux fragment. This identifies the first fragment. Subsequent pixels are compared to their neighbors: where the pixel represents a local maximum it is given a new label; otherwise it is given the label of its greatest neighbor. In this manner, region labels are propagated "downhill".

This technique identifies flux fragments as distinct, even where they are consistent within the noise level. Also, it may return fragments too small to be meaningful in the context of a given investigation. To deal with this, a merging algorithm was included. This first performed "saddle-point" merging, where two fragments were merged if one of the peaks was consistent with the greatest point on the boundary between them. Since merging fragments in different orders can produce different results, the smallest differences between peak and saddle were resolved first. Next, fragments were merged with their least greater neighbor if their area fell below a given threshold. This was then repeated according to flux. In each merging stage, fragments were merged regardless of polarity. Furthermore, in the area and flux merging stages, fragments satisfying the merging criterion, but with no neighbors with which they could be merged, were discarded.

For tessellation purposes, the full disk magnetograms were cropped by visual inspection, using a rectangular template. In some cases, flux identified with other active regions protruded into the sample. This was resolved by setting the affected parts of the magnetogram to zero. To validate the selection, the balance of positive and negative flux was established. The imbalance was typically well less than 30% of the total unsigned flux in the active region. In the cases where the imbalance was so large, fine structures associated with supergranulation were frequently the cause. Where a large imbalance was obtained without such an explanation, the data were discarded.

The threshold values we used for tessellation were 25 G (tessellation), 3 G (saddle merging), 4 pixels (area merging), and 0 Mx (flux merging). The tessellation threshold was set at three times the maximum noise level so as to remove flux not associated with the AR of interest. The saddle-merging threshold was set at the three-sigma level of the average noise to be very sure that flux fragments identified as distinct are such. The area merging threshold was set at four pixels to make the identified fragments larger than the minimum

resolution. With these considerations, it was decided that flux merging was unnecessary.

Inevitably, some real flux fragments will be missed by the tessellation shown in Fig. 1. Two causes are the finite resolution of the magnetogram (fragments too small to be seen) and the tessellation threshold (pixels in which B_{los} falls below 25 G are ignored). To indicate the magnitude of these two effects, Fig. 2 shows the average field within each fragment versus flux content (Abramenko and Longcope 2005). There are two indicators that the data are compromised below a certain flux value. The first is the diagonal stripe pattern seen at low flux values. This is a consequence of pixelation of the magnetogram. The second is the near-absence of points below a limit curving up from 25 G average magnetic field strength. This demonstrates that the data have indeed been compromised by the tessellation threshold. We therefore analyze the data only above flux cutoff $\sim 7.5 \times 10^{18}$ Mx in this paper.

In Fig. 2, the five concentrations in which average magnetic field falls below 25G result from an artifact of the tessellation code where positive and negative flux at the edge of the cropped magnetogram were identified as parts of a single fragment. This is rare (in this study five concentrations in 7428) and such concentrations are removed by the flux cutoff.

Because umbral areas of sunspots are lognormally distributed (Bogdan *et al.* 1988), fragment flux values might be, as well (Abramenko and Longcope 2005). The variance s^2 of $ln\Phi$ values is proportional to the number of independent fragmentations that produce a given fragment (Monin and Yaglom 1975). One could fit the probability distribution function $f(ln\Phi)$ of fragments in each active region with a Gaussian; then s would be given by the Gaussian width. However, this technique depends on binning and the Gaussian width determined in this flawed manner varies significantly with the choice of binning. Following Abramenko and Longcope (2005), we use the cumulative distribution function

$$F_G(ln\Phi) = \frac{1 - erf[(ln\Phi - m)/(s\sqrt{2})]}{1 - erf[(ln\Phi_{cut} - m)/(s\sqrt{2})]}$$

which assumes a Gaussian $f(ln\Phi)$ with a sharp lower cutoff, and has no dependence on binning. The resulting value of s was found to vary little as the value of the flux cutoff was increased, validating the choice of 7.5×10^{18} Mx. Fig. 3 shows the fit of this function to the observed cumulative distribution for AR 9684.

We employed the Kolmogorov-Smirnov (K-S) test to assess the quality of fit for each of the 59 active regions. The median significance was 98%, where 100% is a perfect fit. This high value shows that the lognormal distribution is a very good approximation to our dataset as a whole. Where the fit has a lower significance, the following polarity is considerably more fragmented than the leading, a well known property of mature active regions (Bray and Loughhead 1979; Zwaan 1981; Canfield 1999).

3. FRAGMENTATION, FLARING, AND FLOWS: CORRELATIONS

To establish the relationships between flux fragmentation, flare energy output, and kinetic helicity of flows surrounding the AR in our dataset, a number of parameters and variables come into play. To evaluate the role of these quantities, we use Kendall's rank correlation coefficient (Siegel 1956). This coefficient quantifies how one parameter increases with another, without assuming any underlying functional form. In particular, it is important not to confuse this coefficient with a linear correlation coefficient derived from a least squares fit to the data of a linear function. A Kendall rank correlation coefficient is accompanied by a probability of occurrence under the null hypothesis, $p(H_0)$, which is the two-sided likelihood that the correlation would arise by arranging points at random. Thus, a compelling correlation will be accompanied by a low value of $p(H_0)$. In all statistical studies, it is important to know whether a correlation between two parameters is due to a mutual correlation with a third parameter. The use of Kendall rank correlation coefficients allows partial correlations to be calculated, *i.e.*, the correlation between two parameters with a third parameter held constant. Partial correlation coefficients are not accompanied by a significance, but they are useful when compared with the associated Kendall coefficient. If the comparison shows that the partial coefficient is significantly less than the Kendall coefficient for a given pair of parameters, when a third parameter is held constant, it means that the parameter that is held constant plays an important role in that correlation.

We start by independently checking the basic finding of Komm and collaborators that active regions with strong flare activity show large values of kinetic helicity density in subsurface flows. Komm and collaborators derived the kinetic helicity density at three different mean depths, 0.9 ± 0.5 Mm, 4.4 ± 1.3 Mm, and 10.2 ± 2.5 Mm. They find that all show the same correlation of flare activity and subsurface flows; the correlation at greatest depth is strongest. Table 1 shows the Kendall coefficients and $p(H_0)$ values for various correlations determined in this paper. The first three rows show that Komm's average kinetic helicity density measurements at all three depths correlate extremely well with the GOES flare energy flux E_f (for correlations with flaring, we did not include regions with $E_f = 0$ – an artifact of truncation). The probability that the correlations could occur by chance when there is no real relationship, given by $p(H_0)$, is extremely small – only 0.00796, 0.0112, and 0.000176 respectively. Hence, we confirm the basic finding of Komm and collaborators (Komm *et al.* 2005); active regions with strong flare activity show large values of kinetic helicity density in subsurface flows at all three depths.

The next four rows show that there is no significant relationship between s^2 and $\langle k \rangle$ at any of the three depths. Nor is there a significant correlation between s^2 and E_f. Further testimony to this point appears in Table 2. The values of the partial coefficients for $\langle k \rangle$

(9.0 Mm), $\langle k \rangle$ (4.4 Mm), and $\langle k \rangle$ (10.2 Mm) with E_f when s^2 is held constant are only slightly less than the respective values of the Kendall coefficients in Table 1, as expected if fragmentation plays no significant role in the relationship between E_f and $\langle k \rangle$ at any depth.

4. CONCLUSIONS

First, we find that the formation and coalescence of fragments of magnetic flux in active regions is dominated by repeated random bifurcation. This conclusion is based on tessellation of magnetograms whose fragment flux distribution is found to be lognormally distributed, with a high degree of certainty. Because our active regions are selected without bias in size or flux, and are sufficient in number (59), we believe that this lognormal distribution of fragment flux is a general property of solar active regions, barring the possibility, previously ruled out by the sunspot area study of Bogdan *et al.* (1998), of solar cycle dependence.

Second, we find that the number of independent random bifurcations of the flux of active regions, proportional to the variance of the lognormal distribution s^2, shows no significant correlation with either (1) the subsurface average kinetic helicity density values $\langle k \rangle$ at any of the three depths derived by Komm *et al.* (2005) using local helioseismology in the vicinity of active regions or (2) their energy output in the form of X-ray flares, E_f. The correlation between flaring and kinetic helicity density reduces only slightly when the number of repeated random bifurcations is held constant (Table 2). Hence, we conclude that fragmentation plays no significant role in the relationship between observed subsurface kinetic helicity density values and flare energy output.

Our demonstration that there is no relationship between the flux fragmentation of an active region and its flare energy output is surprising only if one believes that complexity, in the form of the number of independent bifurcations measured by s^2, plays a role in flaring. We know of no compelling statistical demonstration of this relationship.

Finally, we confirm the relationship discovered by Komm *et al.* (2005) between their measured $\langle k \rangle$ values in the upper convection zone and energy output in the form of X-ray flares. If we take this relationship to be indicative of a real physical cause and effect relationship between these two quantities, we are inclined to believe that it is due to the effect of the measured average helical motions on the generation of the components of magnetic helicity that are thought to play a role in flares and coronal mass ejections (Moon *et al.* 2002; Nindos and Andrews 2004; Leka *et al.* 2005; Longcope *et al.* 2007). Such a relationship is quite plausible, in view of the large spatial scale of the averaging (15° in Carrington longitude) that is inherent in the helioseismology methods (Hill 1988; Haber *et al.* 2000) used in the

Komm *et al*. (2005) work. Their averaging scale (horizontally) is more than an order of magnitude larger than the diameter of either a convective cell (Spruit 1974) or an Ω loop (Fan 2004) at the relevant depths in models of the solar convection zone, and therefore much more likely to lead to distortion (and hence twist and writhe generation) than fragmentation.

We thank Dana Longcope, Dibyendu Nandi, and Adam Calhoun for their advice during this project. We thank Rudolf Komm for furnishing tables of the mean kinetic helicity values. We thank the referee for carefully reading the manuscript. The participation of A.J.B.R. was made possible by the MSU Solar Research Experiences for Undergraduates Program and supported by internal MSU funds.

REFERENCES

Abramenko, V. I. and Longcope, D. W. (2005). *ApJ* **619**, 1160.

Barnes, G., Longcope, D. W., and Leka, K. D. (2005). *ApJ* **629**, 561.

Bogdan, T. J., Gilman, P. A., Lerche, I., and Howard, R. (1988). *ApJ* **327**, 451.

Bray, R. J. and Loughhead, R. E. (1979). *Sunspots*. Dover, New York.

Brown, M. R., Canfield, R. C., and Pevtsov, A. A. (1999). *Magnetic Helicity in Space and Laboratory Plasmas*. American Geophsical Union, Washington DC.

Canfield, R. C. (1999). In Priest, E., editor, *Encyclopedia of Astronomy and Astrophysics*, pp. 361–370. Nature Publishing.

Fan, Y. (2004). *Living Reviews in Solar Physics* **1**, 1.

Fan, Y., Fisher, G. H., and Deluca, E. E. (1993). *ApJ* **405**, 390.

Fisher, G. H., Fan, Y., Longcope, D. W., Linton, M. G., and Pevtsov, A. A. (2000). *Solar Phys.* **192**, 119.

Haber, D. A., Hindman, B. W., Toomre, J., Bogart, R. S., Thompson, M. J., and Hill, F. (2000). *Solar Phys.* **192**, 335.

Hill, F. (1988). *ApJ* **333**, 996.

Komm, R., Howe, R., Hill, F., González Hernández, I., and Toner, C. (2005). *ApJ* **630**, 1184.

Leka, K. D., Fan, Y., and Barnes, G. (2005). *ApJ* **626**, 1091.

Longcope, D. W., Beveridge, C., Qiu, J., Ravindra, B., Barnes, G., and Dasso, S. (2007). *Solar Phys.* **in press**.

Longcope, D. W., Fisher, G. H., and Pevtsov, A. A. (1998). *ApJ* **507**, 417.

Monin, A. S. and Yaglom, A. M. (1975). *Statistical Fluid Mechanics: Mechanics of Turbulence*, volume 2. MIT Press, Cambridge.

Moon, Y.-J., Chae, J., Choe, G. S., Wang, H., Park, Y. D., Yun, H. S., Yurchyshyn, V., and Goode, P. R. (2002). *ApJ* **574**, 1066.

Nandy, D. (2006). *JGR* **111**(A10), 12.

Nandy, D., Hahn, M., Canfield, R. C., and Longcope, D. W. (2003). *ApJ* **597**, L73.

Nindos, A. and Andrews, M. D. (2004). *ApJ* **616**, L175.

Schrijver, C. J., Hagenaar, H. J., and Title, A. M. (1997). *ApJ* **475**, 328.

Siegel, S. (1956). *Nonparametric Statistics for the Behavioral Sciences*. McGraw-Hill, New York.

Spruit, H. C. (1974). *Solar Phys.* **34**, 277.

Zwaan, C. (1981). In Jordan, S., editor, *The Sun as a Star*, pp. 163–179.

Table 1. Kendall Rank Correlation Coefficients

Param. A	Param. B	Coefficient	$p(H_0)$
$\langle k \rangle$ (0.9 Mm)	E_f	0.319	0.00796
$\langle k \rangle$ (4.4 Mm)	E_f	0.304	0.0112
$\langle k \rangle$ (10.2 Mm)	E_f	0.451	0.000176
s^2	$\langle k \rangle$ (0.9 Mm)	0.0701	0.432
s^2	$\langle k \rangle$ (4.4 Mm)	-0.00818	0.927
s^2	$\langle k \rangle$ (10.2 Mm)	0.0608	0.496
s^2	E_f	0.105	0.381

Table 2. Partial Coefficients

Param. A	Param. B	Const. Parameter	Coefficient
$\langle k \rangle$ (0.9 Mm)	E_f	s^2	0.307
$\langle k \rangle$ (4.4 Mm)	E_f	s^2	0.298
$\langle k \rangle$ (10.2 Mm)	E_f	s^2	0.441

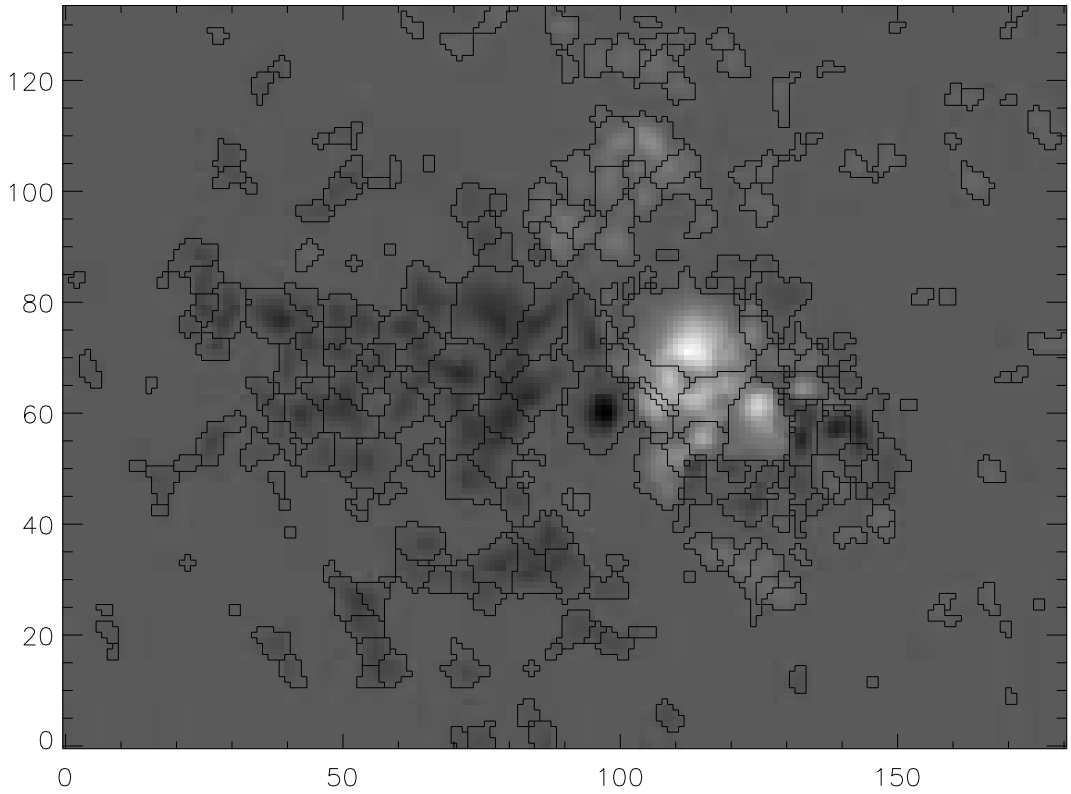

Fig. 1.— A Kitt Peak Vacuum Telescope magnetogram of NOAA AR 9684 after tessellation with the parameters used in this paper (Section 2.1). Positive flux is white; the coordinates are NSO/KP VT pixel indices relative to the origin of the cropped magnetogram.

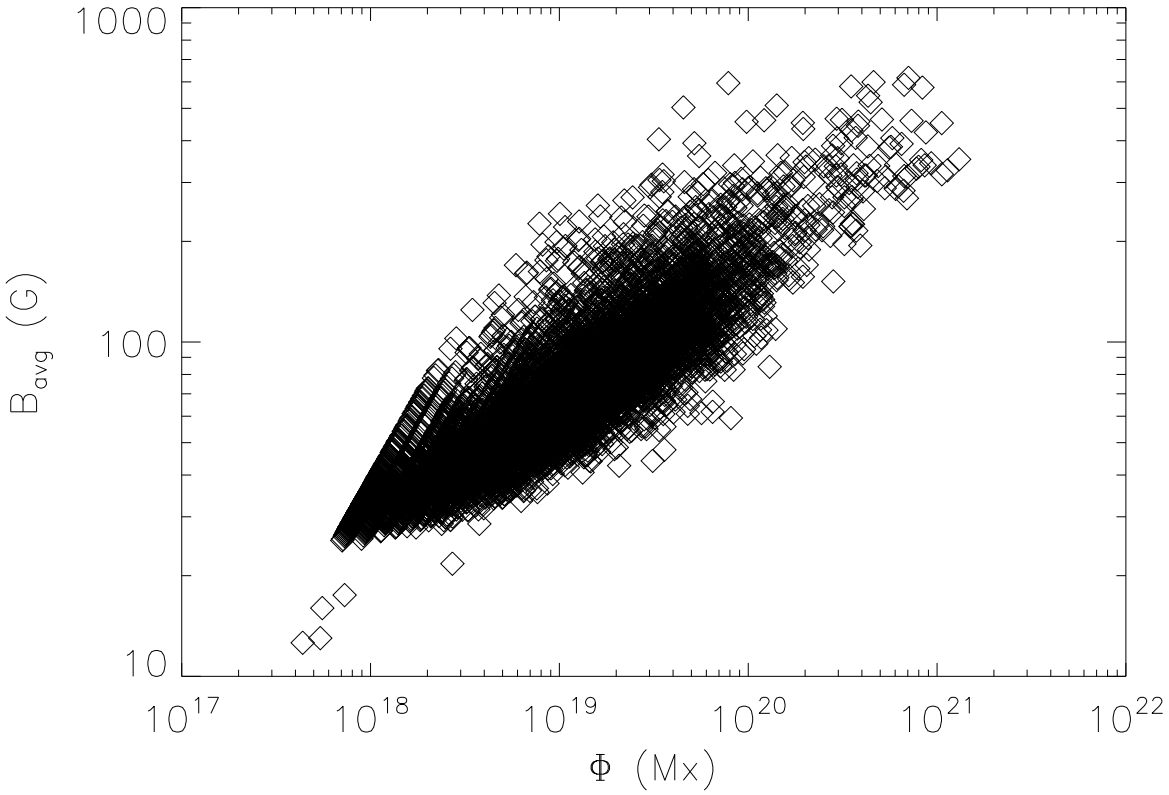

Fig. 2.— Average magnetic field B_{avg} (G) in fragments versus their flux content Φ (Mx), for AR 9684.

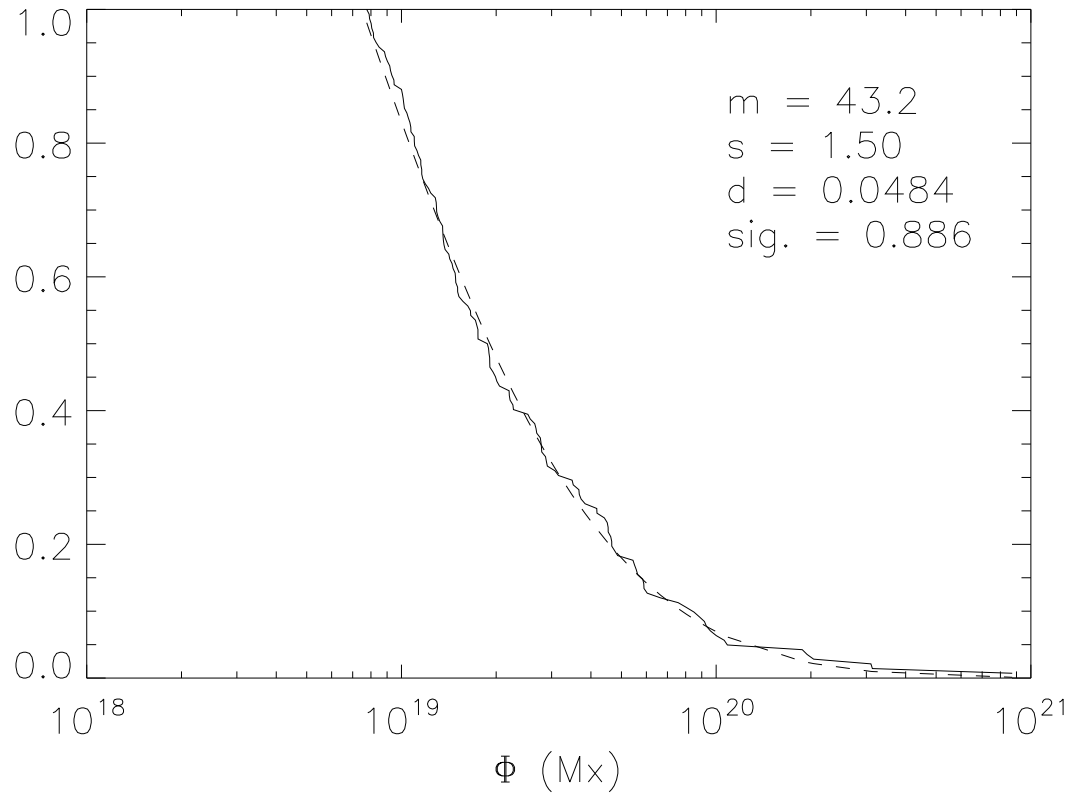

Fig. 3.— The observed cumulative distribution $F(ln\Phi)$ and the best fit cut-Gaussian $F_G(ln\Phi)$ (dashed curve) for AR 9684. The quantities m and s are parameters of $F_G(ln\Phi)$; d and significance (sig.) are parameters of the K-S test.